Strange attractors induced by melting in systems with nonreciprocal effective interactions

Nikita P. Kryuchkov,[1,*] Lukiya A. Mistryukova [ORCID],[1] Andrei V. Sapelkin,[2] and Stanislav O. Yurchenko [ORCID][1,†]

[1]*Bauman Moscow State Technical University, 2nd Baumanskaya Street 5, 105005 Moscow, Russia*
[2]*School of Physics and Astronomy, Queen Mary University of London, London E1 4NS, United Kingdom*

Newton's third law—the action-reaction symmetry—can be violated for effective interbody forces in open and nonequilibrium systems that are ubiquitous in areas as diverse as complex plasmas, colloidal suspensions, active and living soft matter, and social behavior. While studying monolayer complex plasma (confined charged particles in an ionized gas) with nonreciprocal interactions mediated by plasma flows, *in silico* we found that an interplay between melting and thermal activation drastically transforms the collective dynamics: the order-disorder transition modifies the system's thermal steady state so that the crystal tends to melt, whereas the fluid tends to freeze, jumping chaotically between the two states. We identified this collective chaotic behavior as strange attractors formed in a monolayer complex plasma and link the strange attractor behavior to the specifics of interparticle interactions.

I. INTRODUCTION

The reciprocity of action and reaction, known as Newton's third law, can be violated for effective interbody forces in open and nonequilibrium (dissipative) systems. The nonreciprocity can play an important role in dynamics of active matter [1,2], as well as in social systems, such as insect swarms [3–6], crabs [7], fish schools [8–10], animal herds [11], and cells [12]. Today these systems are in the spotlight of intensive studies with collective phenomena that can be in principle observed being one of the central questions. However, the role of nonreciprocity of interactions in such systems remains poorly understood.

Complex plasmas and colloidal systems—microparticles immersed in an ionized gas or solvent, which can be imaged using video recording [13,14]—can also exhibit effective nonreciprocal interactions. The action-reaction symmetry in these systems is broken if the interactions are mediated by a nonequilibrium environment, e.g., flows [14–18], optical beams [19], diffusiophoresis [20–22], and plasma wakes [23–30]. In particular, complex (dusty) plasmas allow detailed studies of different generic phenomena inherent for strongly coupled (condensed) matter to gain insights into physics of fluids, glasses, and crystals [31], including melting and crystallization [32–34], spinodal decomposition [35–37], viscoelastic behavior [38,39], microphysics of fluids [40–42], and excitations and correlations [43–47].

Typical experiments with monolayer dusty plasmas are performed with microparticles injected in a capacitively coupled radio frequency discharge and levitating above the electrode due to the balance of gravity and electric forces [13]. The vertical plasma flow focused downstream of each particle

forms plasma wakes, resulting in nonreciprocal interactions between the particles. This has been shown to change drastically dynamics of dissipative systems (governed by the energy release and dissipation [48]), leading to multiple-temperature steady states [14], single- and double-step thermal activation [49–51], thermoacoustic instability [52], and bistability [53]. The significance of these studies extends well beyond the immediate area of complex plasma, since the corresponding conclusions reveal physical mechanisms governing collective behavior of dissipative systems in general. However, systematic and continuous variation of key parameters that affect system's dynamic behavior in the specific range of interest is frequently limited by technical challenges.

To overcome these limitations and inspired by our recent works [46–52] on dynamics of (confined) monolayer dusty plasma, in this article, we utilize molecular dynamics (MD) simulations and the balance method [48] for analysis of the energy release and dissipation. As a result, we obtained and investigated the dissipative phase diagrams and have analyzed the system's dynamics as a function of confinement strength. We found that, in strong confinement, the system exhibits dissipative spinodal decomposition with the (dissipative) critical point above the melting line in the average kinetic energy of particles. However, starting from the critical confinement strength, the energy release develops a gap during melting. If a steady state falls into the gap, the system becomes frustrated and falls into chaotic jumping between the crystal and fluid, eliciting *strange attractors*.

II. METHODS

A. Details of MD simulations

As a model system capable of melting and thermal activation, we considered a (confined) monolayer of charged microparticles in plasma flow. In our model system particles

*kruchkov_nkt@mail.ru
†st.yurchenko@mail.ru
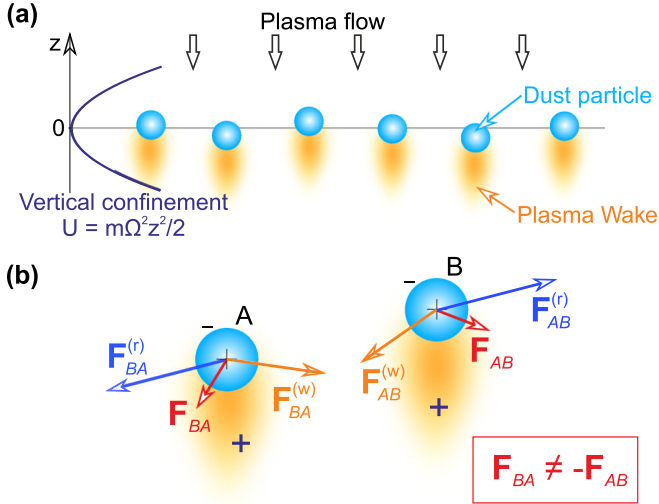
(a)

(b)

$$F_{BA} \neq -F_{AB}$$

FIG. 1. *The schematic illustration of the model system under the study:* (a) The side view of the dust particle monolayer confined in the vertical parabolic potential well. The direction of the plasma flow is indicated by the arrows, and the wakes are shown by the orange clouds. (b) Two negatively charged particles (colored in blue) in plasma flow interact nonreciprocally due to the positively charged wakes (orange clouds). $\mathbf{F}_{AB}^{(r)} = -\mathbf{F}_{BA}^{(r)}$ are the reciprocal (repulsive) forces; $\mathbf{F}_{AB}^{(w)} \neq -\mathbf{F}_{BA}^{(w)}$ denote attractive interactions between (negatively charged) particles and (positively charged) wakes. As result, the particle-wake interactions affect the reciprocity of action and reaction for effective forces, $\mathbf{F}_{BA} \neq -\mathbf{F}_{AB}$.

interact through Yukawa (Debay-Huckel) repulsion, whereas the nonreciprocity is provided by the wakes (in the plasma flow) downstream the particles. We used the smoothed point-wake model (with experimentally relevant parameters), the particles were placed in a parabolic potential well, and the simulations were performed with the Langevin thermostat, in the same manner as in Refs. [49,50,52]; the details are provided below.

The system was set up as a monolayer of charged monodispersed (identical) dusty particles in plasma flow, as illustrated in Fig. 1(a). In this configuration plasma wakes formed downstream the particles are playing the role of the third body, and the forces of action and reaction have different magnitudes and are not collinear [48–50,52] [see sketch in Fig. 1(b)].

MD simulations were performed using the following potential of interparticle interaction [49–52]:

$$\varphi(\mathbf{r}) = \varepsilon \left[\frac{e^{-r/\lambda}}{r/\lambda} - \widetilde{q} \frac{e^{-r_w/\lambda}}{r_w/\lambda} \left(1 + b \frac{e^{-r_w/\lambda}}{r_w/\lambda} \right)^{-1} \right], \quad (1)$$

where $\varphi(\mathbf{r})$ is the potential of the ith particle in the field of the jth particle and its wake, $\mathbf{r}$ is the position vector between the particles, $r_w = |\mathbf{r} - h\mathbf{e}_z|$ is the distance from the particle to the wake, $\mathbf{e}_z$ is the unit vertical z vector, λ is the Debye screening length, $\widetilde{q} = 0.3$ and $h = 0.343\lambda$ are effective wake charge and length, respectively, $b = 1$ is the dimensionless cutoff used to truncate (artificial) divergence of the particle-wake interactions, $\varepsilon = e^2 Z^2 / 4\pi\varepsilon_0\lambda$ is the interaction magnitude determined by the particle charge number Z, and ε_0 is the electric constant. Typically, in experiments we have the charge

number $Z = (1.5 \ldots 2) \times 10^4$, the interparticle distances in crystal $\Delta = (490 \ldots 550) \, \mu$m, and the screening parameters $\kappa = \Delta/\lambda \simeq (1.0 \ldots 1.2)$ [51].

Despite the real interactions between particles in plasma flows being much more complicated than given by Eq. (1) and strongly depend on the plasma parameters [28], Eq. (1) describes in detail a broad range of generic activation phenomena, inherent to systems with nonreciprocal interactions, and has been shown to describe well a range of experimentally observed phenomena such as activated melting in crystals [49,51], thermoacoustic instability in fluid complex plasma [52], and double-step defect activation [50].

In our simulations, the particles were confined in the potential well

$$U(z) = \frac{1}{2} m\Omega^2 z^2, \quad (2)$$

where m is the particle mass, and Ω is the confinement frequency, related to the vertical oscillations of the system in the long-wavelength limit [51]. The strength of vertical confinement is determined by the frequency Ω and can change the spectra of collective excitations and trigger mode-coupling instabilities in plasma crystals and fluids [51,54–56]. Since the system is open (and thus nonconservative), the energy can transfer from the plasma stream into the kinetic energy of microparticles. Note that constant forces, e.g., ion-drag force (related to the interaction of a particle with its wake) and gravity force, can be excluded from consideration: in the potential well (2), these forces only induce an equal offset of the equilibrium vertical position of all particles in monolayer and do not change the interactions between particles [13].

The Langevin equation was used to analyze the dynamics of the many-body system

$$m\dot{\mathbf{v}}_i = \mathbf{F}_i - m\tau^{-1}\mathbf{v}_i + \sqrt{2mT_{\text{th}}/\tau}\,\mathbf{R}_i(t), \quad (3)$$

where $\mathbf{v}_i$, is the velocity of ith particle, $\mathbf{F}_i$ is a total force acting on the ith particle due to the external (confinement) fields and interparticle interactions, τ is a damping time, T_{th} is the temperature of thermostat, and $\mathbf{R}(t)$ is a random force with zero moment $\langle \mathbf{R}_i(t) \rangle = \mathbf{0}$ and δ correlation function $\langle R_{i\alpha}(t)R_{j\beta}(t') \rangle = \delta_{\alpha\beta}\delta_{ij}\delta(t - t')$, where indices α and β denote coordinate axes.

The particles were placed in a rectangular simulation box with infinite size along the z direction and periodic boundary conditions in the x and y directions. A monolayer hexagonal crystal in the plane $z = 0$, with the lattice constant $\Delta = 1.143\lambda$ (relevant to the values in most experiments [13,31,51]), was set as initial configuration. The initial particle velocities were randomly generated in accordance with a Maxwell distribution. The simulations were performed for $N = 10^4$ particles at different temperatures T_{th}. The cutoff radius r_c and time step Δt were set equal to 8λ and $2.5 \times 10^{-3}\sqrt{m\lambda^2/\varepsilon}$, respectively. The number of time steps in simulations was varied from 10^5 to 2×10^7 steps.

Simulations were performed in dimensionless units where lengths, energies, and masses were measured in λ, ε, and m (in this case, the dimensionless frequency Ω is normalized to $\sqrt{\varepsilon/m\lambda^2}$). From a computational point of view these were
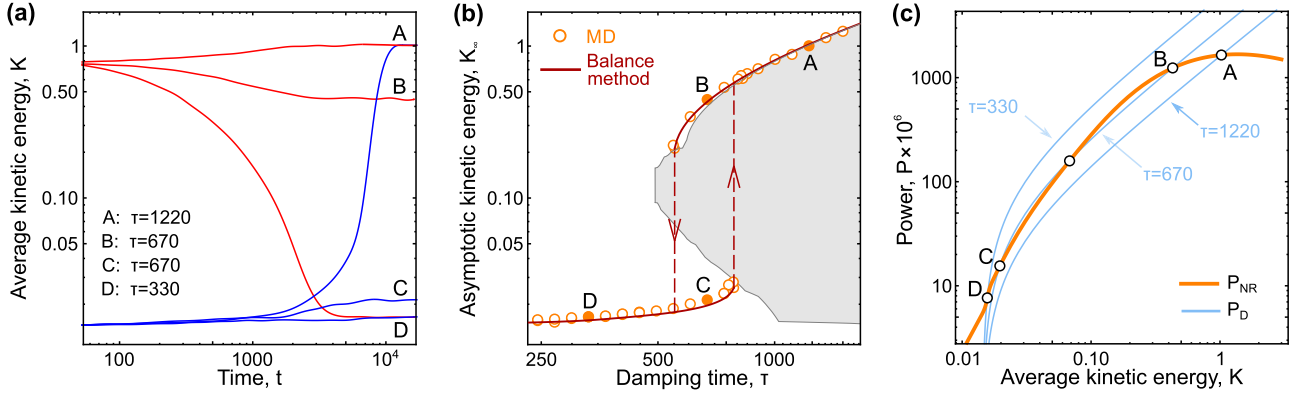
FIG. 2. *The hysteretic behavior of the average kinetic energy in the system at $\Omega^2 = 11.25$ and $T_{\rm th}/T_m = 0.85$: (a) The time evolution of the energy $K(t)$ from "cold" and "hot" initial states, shown by the blue and red solid lines, at different values of τ. (b) The hysteretic dependence of the asymptotic energy K_∞ on the damping time τ. The orange symbols are MD data, the solid red lines are obtained with the balance method [48]. The gray area corresponds to the domain of thermally unstable states [there are no steady states here; the same domain is shown in Fig. 3(a)]. (c) The calculated powers $P_{\rm NR}(K)$ (the orange thick line) and $P_D(K)$ (the blue lines at $\tau = 330$, 670, and 1220) versus the kinetic energy K. The curves and states corresponding to the same conditions are labeled by the same letters A–D (stable states), whereas the state E is unstable.*

equal to $\lambda = 1$, $\varepsilon = 1$, and $m = 1$. All simulations were performed in HOOMD-blue package [57,58].

B. Balance method for analysis of steady states

The balance method was developed in Ref. [48] for effective and detailed analysis of steady states in systems with nonreciprocal interactions. Within this approach the powers of the energy release $P_{\rm NR}$ (due to the nonreciprocity of interactions) and the energy exchange with the thermostat P_D are equal (balanced) in a steady state. The time evolution of the total energy is governed by the equation $\dot{H} = P_{\rm NR} - P_D$, where H is the total energy of the system per particle, consisting of kinetic and potential terms. From the dynamical point of view, a steady state plays the role of a normal attractor, while the balance method allows one to calculate easily corresponding dissipative phase diagrams.

The power $P_{\rm NR}$ is obtained with MD simulations without damping ($\tau \to \infty$) followed by the calculation of [48]

$$P_{\rm NR} = \langle \mathbf{v} \cdot \mathbf{F} \rangle, \tag{4}$$

where $\langle \cdot \rangle$ denotes the ensemble averaging. During the simulations, we scaled the particle velocities every 200 time steps in order to hold the average kinetic energy per particle K at a given value, to obtain $P_{\rm NR}(K)$.

In the framework of the balance method [48], the velocity distribution is assumed to be almost Maxwellian (that corresponds to the most states observed in MD simulations), and, hence, the power P_D is

$$P_D = 2\tau^{-1}\left(K - \frac{3}{2}T_{\rm th}\right). \tag{5}$$

In Fig. 2 we illustrated an example of analysis with the balance method at $T_{\rm th}/T_m = 0.85$ and $\Omega^2 = 11.25$ (here T_m is the melting temperature of the 2D Yukawa crystal with the same screening parameter $\kappa = \Delta/\lambda = 1.143$ as was used in MD simulations [59]). The time evolution of the energy $K(t)$, obtained with MD simulations at different τ, is shown

in Fig. 2(a) by the solid blue and red lines for the high- and low-energy initial states. The asymptotic energies K_∞ (at $t \to \infty$), corresponding to the steady states at different τ, are shown in Fig. 2(b) by the orange symbols for MD results, whereas the solid red line was obtained with the balance method. At small and large τ, the asymptotic behavior does not depend on the initial state, whereas the hysteretic loop is observed at intermediate τ values, similarly to that in Ref. [48]. The calculated powers $P_{\rm NR}$ and P_D are shown in Fig. 2(c) by the thick orange and blue lines (at different τ values) versus the energy K. Depending on the character of intersection, the states with $P_{\rm NR} = P_D$ can be stable (the states A–D) or unstable, as the state E in Fig. 2(c). The states given by the balance method agree excellently with MD simulations, while the method is essentially less time consuming numerically and allows deep theoretical analysis at different τ and $T_{\rm th}/T_m$. As shown in Fig. 2(b), the system can be in nonactivated or activated states with limit points, where corresponding curves $K_\infty(\tau)$ in $\tau - K$ plane are cut off (on the left and right side if the hysteretic loop). The set of limit points obtained at different thermostat temperatures form the boundary of the gray-colored domain (domain of thermal instability): The system does not have any steady states with τ and K belonging to the gray-colored domain.

C. Calculation of excitation spectra

To obtain the spectra of excitations, we used an approach based on the analysis of the velocity current $\mathbf{j}(\mathbf{q}, t)$ [60,61]

$$\mathbf{j}(\mathbf{q}, t) = N^{-1}\sum_s \mathbf{v}_s(t) \exp[i\mathbf{q}\mathbf{r}_s(t)], \tag{6}$$

where $\mathbf{q}$ is the wave vector, and N is the total number of particles in the region of analysis. The excitation spectrum for a mode ξ with the polarization vector $\mathbf{e}_\xi$ (we assume that $\mathbf{e}_\mu \cdot \mathbf{e}_\nu = \delta_{\mu\nu}$) can be calculated with the Fourier transform

$$C_\xi(\mathbf{q}, \omega) = \int dt\, e^{i\omega t}\mathrm{Re}\langle j_\xi(\mathbf{q}, t)j_\xi(-\mathbf{q}, 0)\rangle, \tag{7}$$
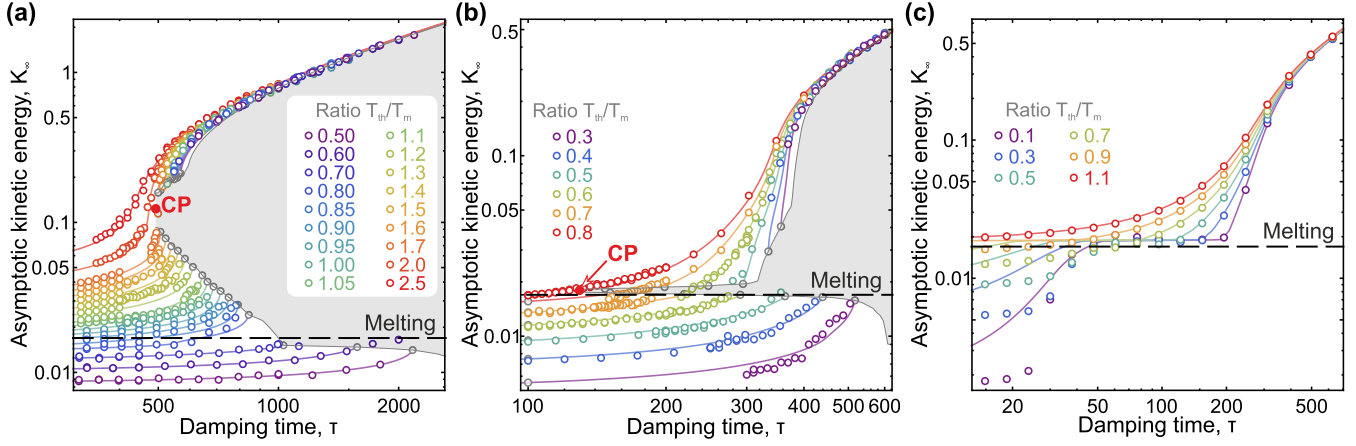
FIG. 3. *Dissipative phase diagrams of the system at different confinement strength*: Panels (a)–(c) correspond to the confinement frequencies $\Omega^2 = 11.25, 9.75$, and 9.0, respectively. The symbols and solid lines are MD data and the results of the balance method, respectively, at different thermostat temperatures T_{th}. The domains of thermally unstable states (there are no steady states here), obtained with the balance method [48], are gray-colored [the gray-colored domain (a) is exactly the same as shown in Fig. 2(b)]. The dashed black lines correspond to the melting, $K_\infty / T_m = 3/2$.

where $j_\xi(\mathbf{q}, t) = \mathbf{j}(\mathbf{q}, t) \cdot \mathbf{e}_\xi$ is the velocity current projection and the brackets $\langle \ldots \rangle$ denote the canonical ensemble average. We used the vectors $\mathbf{e}_v = \mathbf{e}_z$, $\mathbf{e}_L = \mathbf{q}/q$, and $\mathbf{e}_T = \mathbf{e}_v \times \mathbf{e}_L$, corresponding to the (optical) out-of-plane mode and the (acoustical) in-plane longitudinal and transverse modes, respectively. In the case of spatially isotropic fluid states, one can average $C_\xi(\mathbf{q}, \omega)$ over the different $\mathbf{q}$ directions in the horizontal plane, to enhance the signal to noise ratio [61].

To analyze the dispersion curves $\omega_\xi(\mathbf{q})$ and the damping rates $\Gamma_\xi(\mathbf{q})$ of the excitations corresponding to the different modes, we used analysis developed in Refs. [47,61,62] and based on fitting of $C_\xi(\mathbf{q}, \omega)$ at different $\mathbf{q}$ values with the Lorentzian

$$C_\xi(\mathbf{q}, \omega) \propto \frac{\Gamma_\xi}{(\omega - \omega_\xi)^2 + \Gamma_\xi^2} + \frac{\Gamma_\xi}{(\omega + \omega_\xi)^2 + \Gamma_\xi^2}. \quad (8)$$

Equation (8) follows from Eq. (7) in assumption that $\langle j_\xi(\mathbf{q}, t) j_\xi(-\mathbf{q}, 0) \rangle \propto e^{-\Gamma t} \cos(\omega t)$ [61].

The separate mode analysis works well in crystals, where the anharmonic effects are weak and, thus, the lifetime of the excitations is large. On the other hand, in fluids, structural disorder and anharmonicity lead to effective interaction between different modes, their hybridization, and spectra redistribution at short wavelengths [47,62]. In this case, one should analyze the total current spectra $C(\mathbf{q}, \omega) = C_v(\mathbf{q}, \omega) + C_L(\mathbf{q}, \omega) + C_T(\mathbf{q}, \omega)$, which are calculated with MD and than should be fitted at each q with the three-oscillator model

$$C(\mathbf{q}, \omega) \propto \sum_\xi \left[\frac{\Gamma_\xi}{(\omega - \omega_\xi)^2 + \Gamma_\xi^2} + \frac{\Gamma_\xi}{(\omega + \omega_\xi)^2 + \Gamma_\xi^2} \right],$$

where the summation is performed over all three polarizations (v, L, and T). This three-oscillator model allows to take into account the effects of mode hybridization at short wavelengths [47,62].

III. ACTIVATION AND MELTING

At the fixed interaction model (described in Sec. II A) and the system's density, its dynamics is determined by the damping time τ, the confinement frequency Ω, and the thermostat temperature T_{th}/T_m (which we normalized to the melting temperature T_m of the corresponding Yukawa 2D crystal [59]). Therefore, to analyze steady states with the balance method, we calculated powers of energy release (due to nonreciprocity of forces) and dissipation (due to the interaction of the system with thermostat) at different τ, Ω, and T_{th}/T_m (see Sec. II B for details). Then, the steady states, where the powers of energy release and dissipation are equal, were obtained in the same manner as illustrated in Figs. 2(b) and 2(c).

The dissipative phase diagrams are shown in Fig. 3, where the asymptotic values of the average kinetic energy per particle K_∞ were obtained at different τ, T_{th}/T_m, and $\Omega^2 = 11.25$, 9.75, 9.0 (characterizing the confinement strength) in panels (a–c), respectively. Here exactly the same kind of plot is shown as in Fig. 2(b), and the curve shown in Fig. 3(a) for $T_{\mathrm{th}}/T_m = 0.85$ is the same as in Fig. 2(b). The dashed black lines correspond to the melting line $K_\infty/T_m = 3/2$, since K plays a role, analogous to temperature. The gray areas (obtained with the balance method) are the domains of *dissipative spinodal decomposition*, where the system is thermally unstable. The dissipative spinodal decomposition, introduced in Ref. [48] for systems with nonreciprocal interactions, means that, with a decrease in thermostat temperature, the system acquires an ability to exist in nonactivated or activated steady states separated by the gap in asymptotic kinetic energy K. This situation is similar to *thermodynamic spinodal decomposition*, in that, with a decrease in temperature below a critical point (e.g., in condensable systems or mixtures), the system becomes decomposed into condensed or gaseous states separated by the gap in density (or concentrations in the case of mixtures). The difference is the dissipative phase transitions does not require attraction or mixture of different particles (as thermodynamic analog) and can occur in the
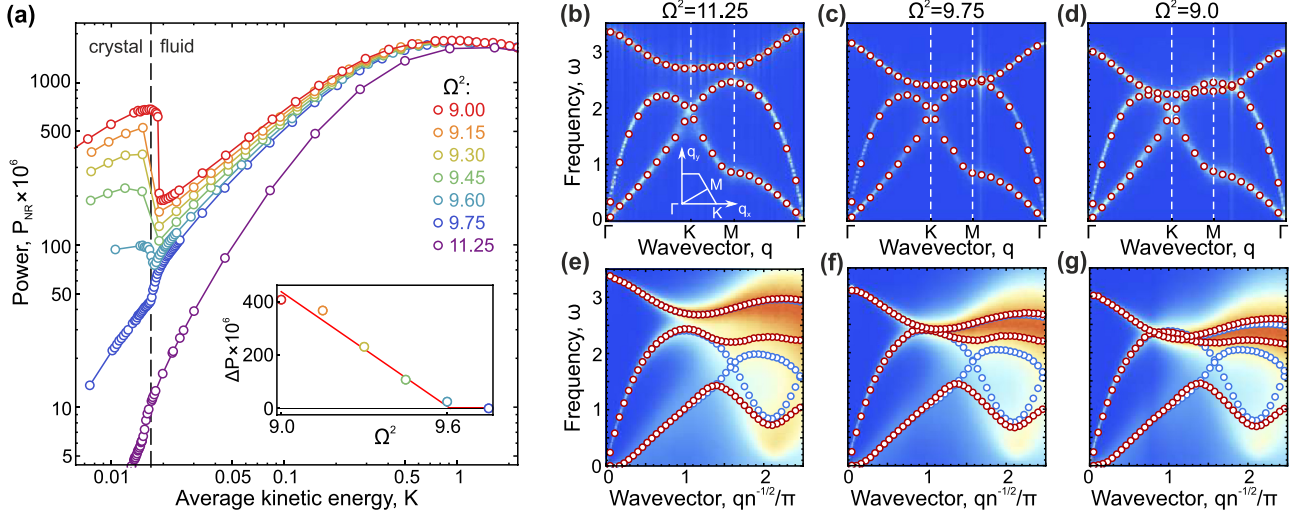
FIG. 4. *The energy release power and the excitation spectra:* (a) Dependencies $P_{NR}(K)$ of the energy release due to the interaction nonreciprocity at different Ω^2. The gap of the energy release power in crystal and fluid ΔP at the melting line is shown in the inset. (b–g) Excitation spectra in crystal (b–d) and fluid (e–g) states. The color-coded velocity current spectra $C(\mathbf{q}, \omega)$ were normalized to the maximum in ΓK intervals in crystal and to the maximum at each q in fluid. The first Brillouin zone in crystal is sketchily shown in (b). The blue symbols are results of single-mode analysis, and red ones are obtained with the three-oscillator model (see details in Sec. II C). The parameters of simulations (for technical details see Sec. II A) are (b) $\Omega^2 = 11.25$, $T_{th}/T_m = 0.6$, $\tau = 240$; (c) $\Omega^2 = 9.75$, $T_{th}/T_m = 0.6$, $\tau = 30$; (d) $\Omega^2 = 9.0$, $T_{th}/T_m = 0.6$, $\tau = 240$; (e) $\Omega^2 = 11.25$, $T_{th}/T_m = 0.9$, $\tau = 730$; (f) $\Omega^2 = 9.75$, $T_{th}/T_m = 0.6$, $\tau = 270$; (g) $\Omega^2 = 9$, $T_{th}/T_m = 0.1$, $\tau = 220$. The energy $K/T_m \simeq 2.4$ in the fluid states (e–g).

system of identical particles with nonreciprocal interactions, as we consider here. The set of steady states with the least K on the activated branches and with the largest K on the nonactivated ones at different thermostat temperatures form in the τ-K plane the dissipative spinodal line, restricting the gray-colored domain with no steady states inside, as illustrated in Fig. 3. The results obtained with MD simulations (the symbols) agree well with those provided with the balance method (the solid lines). The discrepancies are observed only at low K_∞ and τ and are caused by the features of the energy release during the crystalline mode-coupling instability [54,55].

Under strong confinement, the system exhibits the dissipative spinodal decomposition between the nonactivated and activated states, with the dissipative critical point (CP), as shown in Fig. 3(a). Depending on the energy $K_\infty/T_m \gtrless 3/2$, the system can exist in a fluid or solid state. The lines with the same T_{th} play a role of isotherms [48], and the dissipative spinodal decomposition is possible only if T_{th} is less than the *critical thermostat temperature*. Because of the dissipative critical point is above the melting line in the energy K_∞, fluid can exist in nonactivated or activated states at $0.8 \lesssim T_{th}/T_m \lesssim 1.6$.

With a decrease in Ω^2, the critical point shifts down to the melting line, as illustrated in Fig. 3(b). Here the energies K_∞ at the critical point and at the melting are practically coincide, and the nonactivated fluid state becomes unstable. Further decrease in Ω^2 changes drastically the phase diagram, as highlighted in Fig. 3(c) for $\Omega^2 = 9$: The averaged energy $K_\infty(\tau)$ acquires the horizontal plateau near the melting line at $T_{th}/T_m \lesssim 0.6$. This suggests significant changes in dynamic behavior of the system between $\Omega^2 = 9.75$ and $\Omega^2 = 9$. To

shed light onto the origins of these changes, we investigated the effect of confinement strength on the excitation spectra of the system and energy release.

IV. EXCITATION SPECTRA AND ENERGY RELEASE

A steady state of a dissipative system is determined by the balance of the energy release and dissipation, provided by the interaction of nonreciprocity and damping in our case [48]. While the damping rate and thermostat temperature control the dissipation, the confinement strength affects the in- and out-of plane excitations in the system, thus affecting the energy release. To understand the mechanisms responsible for the behavior shown in Fig. 3, we calculated the dependencies of the energy release power $P_{NR}(K)$ as a function of energy K together with the excitation spectra of the crystals and fluids [47,61–63] (see details in Secs. II B and II C) at different Ω^2.

The energy release power is shown in Fig. 4(a) at different Ω^2, with the dashed black line indicating the melting line of the 2D Yukawa crystal [59] with the same parameters of interaction as we used in present work (see Sec. II A). The gap ΔP between the energy release power in crystal and fluid at the melting line [calculated as the maximal drop in P_{NR} between the neighboring points in Fig. 4(a)] is shown in the inset. One can see that the energy release becomes suppressed (in crystal) at $\Omega^2 > \Omega_*^2 \simeq 9.5$, P_{NR} increases monotonously with K, and $\Delta P = 0$ (there is no drop in P_{NR} with melting of the crystal). On the other hand, ΔP becomes positive at $\Omega^2 \lesssim \Omega_*^2$ and changes approximately linearly near the threshold, as shown by the solid red line in the inset in Fig. 4(a). In this range of Ω^2 the energy release in the crystal becomes
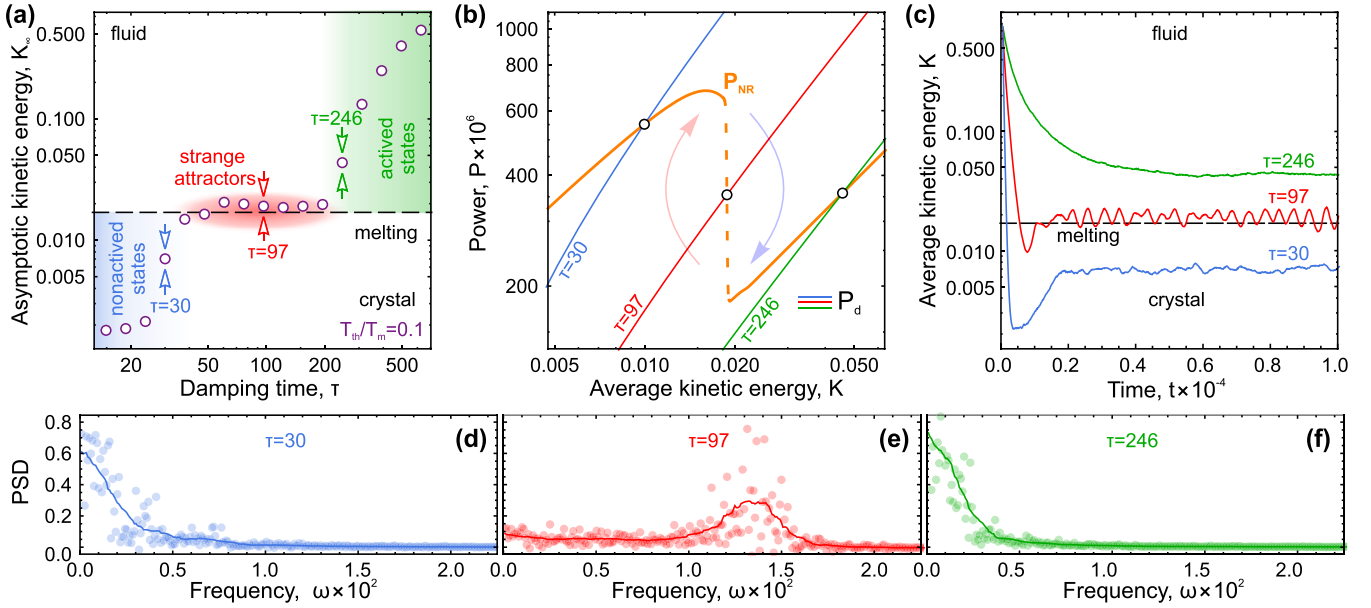
FIG. 5. *Strange dynamic attractor:* (a) The dependence of kinetic energy $K_\infty(\tau)$ on the damping time τ at $T_{th}/T_m = 0.1$ and $\Omega^2 = 9.0$. (b) The power of energy release $P_{NR}(K)$ (thick orange line) and dissipation $P_d(K)$ at $\tau = 30$, 97, and 246 (blue, red, and green lines), under the same conditions as in (a). At $\tau = 97$, the steady state should have been in the gap shown by the dashed vertical line; as a result, the system is forced to oscillate around the point, as justified in panel (c) for dependencies $K(t)$ at $\tau = 30$, 97, and 246. (d–f) Power spectrum densities of $K(t)$ at the same τ values as in (c).

significantly larger (and grows steadily as $\Omega^2 \to 9.0$) than in the fluid, leading to $\Delta P > 0$: this means that, under the same conditions, the crystal is thermally activated, whereas the fluid is not. At $\Omega^2 = \Omega_*^2$, the energy release in crystal and fluid become equal at the melting line.

Further insights into observed behavior can be gained from the dispersion relations $\omega(q)$ for excitations in crystals and fluids, shown in Figs. 4(b)–4(g). At strong confinement, the (optical) out-of-plane and (acoustic) in-plane longitudinal branches do not intersect, as seen in Figs. 4(b) and 4(e). However, as Ω^2 is reduced and approaches to the threshold $\Omega^2 = \Omega_*^2$, the modes touch and then cross, contributing to the enhanced energy release due to their interaction, generally inherent for the nonreciprocal systems [51,54–56], as illustrated in Figs. 4(c) and 4(d) and 4(f) and 4(g). To obtain the spectra, we used single-mode analysis (separate fitting of the modes) and a more accurate three-oscillator model (for joint fitting) [61] (see details in Sec. II C). The spectra are shown by the blue and red symbols in Figs. 4(c)–4(g). The results obtained with the different approaches agree well in crystal and at small q. At $qn^{-1/2}/\pi \gtrsim 1.5$, we observe the anticrossing between the longitudinal and transverse in-plane modes in fluid (in total agreement with Refs. [47,62]) when the excitation branches repel in frequencies and become hybridized. Thus, growth of the gap ΔP in the energy release power is correlated with the crossing between optical and longitudinal acoustic modes in the fluid, which is, in turn, responsible for the principal change of the dissipative phase diagram illustrated in Figs. 3(b) and 3(c) at at $\Omega^2 = \Omega_*^2$. In fact, as we show below, the gap ΔP in the power $P_{NR}(K)$ as a result of melting leads to *emergent dynamic behavior* of the system (in the dynamics of the average kinetic energy K)—the *strange attractor*.

V. THE STRANGE ATTRACTOR

Development of the gap ΔP in the energy release power results in the energy ($K(t)$) fluctuation around the plateau observed in Fig. 3(c), corresponding to the dynamic strange attractors elicited by the "interference" of the activation and melting. This is illustrated in Fig. 5, where Fig. 5(a) reproduces the same data for $K_\infty(\tau)$ at $T_{th}/T_m = 0.1$ as in Fig. 3(c), with the plateau in the range $40 \lesssim \tau \lesssim 200$. The dependencies of the energy release power $P_{NR}(K)$ and dissipation $P_d(K)$ (at different τ) are shown in Fig. 5(b). We considered three representative values of $\tau = 30$, 97, and 246, with the corresponding lines and points in blue, red, and green, respectively, in Fig. 5. As seen in Fig. 5(b), at small and large τ, P_{NR} and P_d cross at one point corresponding to the steady state. However, at τ corresponding to the plateau in Fig. 5(a), the steady state should have been in the gap, as shown in Fig. 5(b) for $\tau = 97$. At this τ both the crystal and fluid become thermally unstable: the (activated) crystal is heated and tends to melt, but the (non-activated) fluid is cooled and tends to freeze. The oscillations of $K(t)$ at $\tau = 97$, shown in Fig. 5(c), stand in contrast with the behavior at $\tau = 30$ and 247. This is further illustrated by the power spectrum densities (PSDs) shown in Figs. 5(d)–5(f), that we calculated as $\text{PSD}(\omega) = \int R(t') \exp(-i\omega t') dt'$, where $R(t') = \langle K(t)K(t+t')\rangle/\langle K(t)^2\rangle$ and the brackets $\langle \cdot \rangle$ denote ensemble average and the relaxation part of $K(t)$ is discarded. The spectral densities are similar at small and large τ, demonstrating only thermal fluctuations and slow relaxation, whereas a broad peak around $\omega \approx 1.35 \times 10^{-2}$ is observed at $\tau = 97$.

The chaotic dynamics can be clearly visualized with representing the dependencies shown in Fig. 5 in the coordinates $\{K, \dot{K}, \dot{H}\}$, where $\dot{H} = P_{NR} - P_d$, in a typical manner for
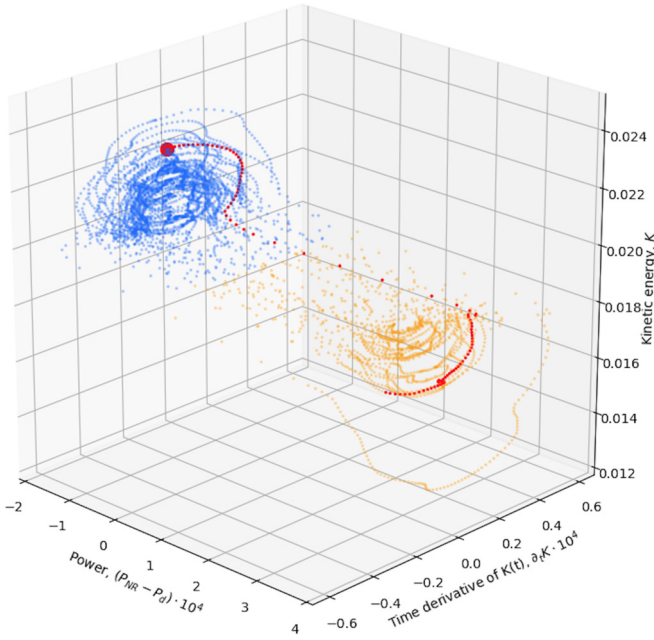
FIG. 6. *Trajectory of the system in the phase space* $\{K, \dot{K}, P_{NR} - P_d\}$: Blue and orange points correspond to (nonactivated) liquid and (activated) crystal, respectively. The red points depict the evolution over previous 300 dimensionless time units. See the supplemental movie [64] for detailed picture of the time evolution.

analysis of nonlinear dynamics [65] (see the supplemental movie [64] and Fig. 6). In Fig. 6 the system states are shown for 5×10^3 (dimensionless) time units: red points represent the last 300 time units, blue and orange points correspond to the nonactivated fluid and activated crystal, respectively. The results in Figs. 5 and 6 clearly and comprehensively evidence strange attractor and reveal the physical mechanism responsible for such behavior: Due to the structural phase transition, the thermal attractor of (nonactivated) fluid turns out to belong to crystalline domain, whereas the crystalline state becomes thermally activated, and its thermal attractor is located above the melting line, in fluid domain. The melting or freezing plays a role of the trigger, which changes the structure, excitation spectra, and position of the thermal attractor. As a result of the dissipative and structural phase transitions overlapping, the system evolution demonstrates strong aperiodic oscillations and chaotic jumps between crystalline and fluid states, revealing the strange attractor.

In addition to the main result, to illustrate that the key reason for chaotic behavior is the irreversible (nonmonotonous) form of the power function P_{NR} provided by melting, one can use the simplified discrete-time model [65]. As a start, consider the time evolution of the total energy, $\dot{H} = P_{NR} - P_d$. In our case, the system oscillates around the melting line, where the heat capacity of the system per particle is $C_V \simeq (2.85 \ldots 3.0)$ and remains practically constant [66]. This means that the oscillations can be considered as harmonic, and corresponding average kinetic and potential terms in the total energy can be assumed to be equal, $H \simeq 2K + M$ [here M is the static (Madelung) energy of the system]. Then we replace the time derivative with the finite difference, as $\dot{H} \simeq 2\dot{K} \simeq$
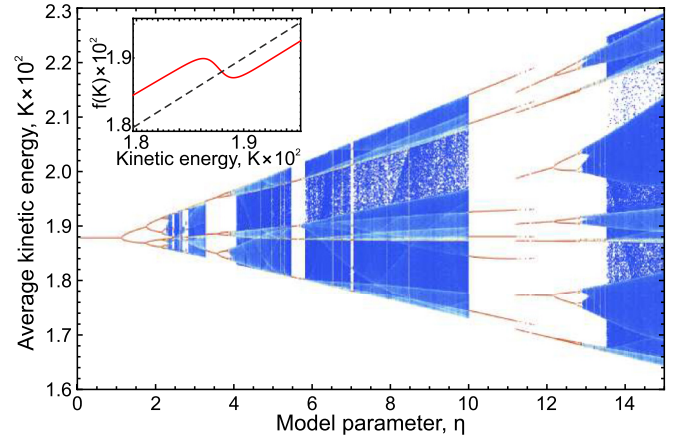

FIG. 7. *The bifurcation diagram of the discrete-time model* (9): The color code represents the relative probabilities of the energy K at fixed η, from blue to red. An example of the mapping function $f(K)$ given by Eq. (9) with $\eta = 1.5$ and $f(K) = K$ are shown by the solid red and dashed gray lines in the inset. The jumps and chaotic behavior arise due to the irreversible (nonmonotonous) form of the mapping function $f(K)$.

$(K_{n+1} - K_n)/\eta$, and obtain the discrete model

$$K_{n+1} = f(K_n), \quad f(K) = K + \eta[P_{NR}(K) - P_d(K)], \quad (9)$$

where K_n is the kinetic energy at the discrete-time moment t_n, $f(K)$ is the mapping function, and η is the step of the discrete-time model, $\eta = (t_{n+1} - t_n)/2$, and 2η should be much smaller than the characteristic time of the kinetic energy evolution [in the case shown in Fig. 5(c), the time is $T = 2\pi/\omega_{max} \simeq 450$, where $\omega_{max} \simeq 1.35 \times 10^{-2}$ is the frequency of the PSD maximum in Fig. 5(e)]. Taking the same powers P_{NR} and P_d as shown in Fig. 5(b) (at $\tau = 97$), we calculated the bifurcation diagram with a standard approach [65]. We performed 5×10^4 iterations by $K_{n+1} = f(K_n)$ to obtain the K_n sequence for each value of η. After that, the last 5×10^3 values of each sequence were plotted. The results in a color-coded format for probabilities (from blue to red for lower and higher ones respectively) are presented in Fig. 7. An example of the function $f(K)$ at $\eta = 1.5$ is shown in the inset with the solid red line.

The classical scenario of transition to chaos through the cascades of period-doubling bifurcations [65] is clearly seen in Fig. 7. The model (9) is rather simple and does not take into account stochastic noise, but allows us to illustrate the main reason leading to the strange attractor formation: This is caused by the form of the mapping function $f(K)$, which is irreversible (nonmonotonous) and, hence, can lead to chaotic behavior with the formation of strange attractors. This means also that the model system we considered can exhibit chaotic jumps between different states, spontaneous melting, and freezing even if we neglect the stochastic nature of the Langevin thermostat.

Note that one can estimate η, corresponding to the strange attractor in Fig. 5 at $\tau = 97$, by comparing the magnitudes of the kinetic energy fluctuations in Figs. 5(c) and 7, which yields $\eta \sim 11$. The step of the discrete model is significantly smaller than characteristic relax-

ation time of the system, $\eta/\tau \simeq 0.11$ and $2\eta/T \simeq 0.05$. This *a posteriori* justifies the suitability of the (simplified) discrete model (9) for qualitative analysis of the nonlinear dynamics in our system. However, one should note that, to describe accurately the system's dynamics, continuous-time stochastic Langevin equations should be solved with MD simulations.

VI. CONCLUSIONS

Utilizing MD simulations, we studied a model many-body system exhibiting thermodynamic and dissipative phase transitions between solid and fluid, as well as thermally activated and nonactivated states. Our results reveal a generic mechanism responsible for chaotic collective behavior—*the strange attractor dynamics*—in the systems capable of thermodynamic and dissipative phase transitions. On melting, the long-range structural correlations are lost, and the spectra of fluctuations change discontinuously. This plays a crucial role in emerging dynamic behavior, since a steady state of a dissipative system is determined by the balance of energy release and dissipation. Due to the change in the structure and in the excitation spectra, the energy release power can acquire a gap between the values in crystal and fluid at the melting line. If the dissipation power falls into the gap, the (activated) crystal is heated and tends to melt, whereas the (nonactivated) fluid is cooled and tends to freeze, eliciting the strange attractor. Thus, for the first time we link the strange attractor behavior to the interactions between individual particles.

We found that the dissipative phase diagrams can be easily calculated with a simple balance method [48]. Although the model system of charged particles with nonreciprocal forces mediated by plasma wakes has been known for a long time, the strange attractors have never been observed or reported, to the best of our knowledge. Strange attractor we identified here might be responsible for unusual dynamics, bistability, and jumps between crystalline and fluid states of monolayer complex plasma that was observed experimentally in Ref. [53], but has never been understood in detail and associated with the nonreciprocity of interactions and interplay between dissipative and structural phase transitions.

Strange attractors, known for a long time in systems with "normal" reciprocal interactions between particles (e.g., in fluids), typically arise in the presence of external driving forces, which do not affect the interparticle interactions. An example is thermal convection (triggered by external heat source) described by the well-known Lorentz model [65]. In the case we considered here, the main reason for the observed behavior is the interaction nonreciprocity, induced due to a nonequilibrium environment (plasma flows).

Provided by the same underlying physics, the strange-attractor-like behavior is expected for a broad range of other systems, whose dynamics can be described by Langevin equation with some effective nonreciprocal forces: for instance, in active colloids and emulsions [2,20–22], in crowding systems with the discontinuous change in the neighboring distribution [1], and in dynamics of patterns and collective behaviors in biology, including insect swarms [3–6], crabs [7], fish schools [8–10], animal herds [11], and cells [12].

Since nonreciprocal interactions are inherent to a plethora of open, nonequilibrium, and artificial systems, we believe the results should be interesting to the broader community in complex plasmas, active soft matter, and living, multiagent, and social systems. The approaches to analysis we used here can be applied in these cases to study self-organization and nonlinear dynamics. Therefore, we hope that our work will stimulate corresponding theoretical studies and experiments.

[1] T. Vicsek and A. Zafeiris, Phys. Rep. **517**, 71 (2012).

[2] C. Bechinger, R. Di Leonardo, H. Löwen, C. Reichhardt, G. Volpe, and G. Volpe, Rev. Mod. Phys. **88**, 045006 (2016).

[3] J. Buhl, D. J. T. Sumpter, I. D. Couzin, J. J. Hale, E. Despland, E. R. Miller, and S. J. Simpson, Science **312**, 1402 (2006).

[4] J. E. Ron, I. Pinkoviezky, E. Fonio, O. Feinerman, and N. S. Gov, PLoS Comput. Biol. **14**, e1006068 (2018).

[5] O. Feinerman, I. Pinkoviezky, A. Gelblum, E. Fonio, and N. S. Gov, Nat. Phys. **14**, 683 (2018).

[6] G. Ariel and A. Ayali, PLoS Comput. Biol. **11**, e1004522 (2015).

[7] Y.-P. Gunji, H. Murakami, T. Tomaru, and V. Basios, Philos. Trans. R. Soc. A **376**, 20170370 (2018).

[8] K. Tunstrøm, Y. Katz, C. C. Ioannou, C. Huepe, M. J. Lutz, and I. D. Couzin, PLoS Comput. Biol. **9**, e1002915 (2013).

[9] A. Filella, F. Nadal, C. Sire, E. Kanso, and C. Eloy, Phys. Rev. Lett. **120**, 198101 (2018).

[10] D. S. Calovi, U. Lopez, S. Ngo, C. Sire, H. Chaté, and G. Theraulaz, New J. Phys. **16**, 015026 (2014).

[11] F. Ginelli, F. Peruani, M.-H. Pillot, H. Chaté, G. Theraulaz, and R. Bon, Proc. Natl. Acad. Sci. USA **112**, 12729 (2015).

[12] K. Copenhagen, G. Malet-Engra, W. Yu, G. Scita, N. Gov, and A. Gopinathan, Sci. Adv. **4**, eaar8483 (2018).

[13] A. Ivlev, H. Löwen, G. Morfill, and C. P. Royall, *Complex Plasmas and Colloidal Dispersions* (World Scientific, Singapore, 2011).

[14] A. V. Ivlev, J. Bartnick, M. Heinen, C.-R. Du, V. Nosenko, and H. Löwen, Phys. Rev. X **5**, 011035 (2015).

[15] J. Dzubiella, H. Löwen, and C. N. Likos, Phys. Rev. Lett. **91**, 248301 (2003).

[16] K. Hayashi and S. ichi Sasa, J. Phys.: Condens. Matter **18**, 2825 (2006).

[17] C. Mejía-Monasterio and G. Oshanin, Soft Matter **7**, 993 (2011).

[18] I. Sriram and E. M. Furst, Soft Matter **8**, 3335 (2012).

[19] K. Dholakia and P. Zemánek, Rev. Mod. Phys. **82**, 1767 (2010).

[20] B. Sabass and U. Seifert, Phys. Rev. Lett. **105**, 218103 (2010).

[21] R. Soto and R. Golestanian, Phys. Rev. Lett. **112**, 068301 (2014).

[22] H. J. Keh, Curr. Opin. Colloid Interface Sci. **24**, 13 (2016).

[23] V. N. Tsytovich, Phys.-Usp. **40**, 53 (1997).

[24] S. A. Khrapak, A. V. Ivlev, and G. Morfill, Phys. Rev. E **64**, 046403 (2001).

[25] M. Chaudhuri, A. V. Ivlev, S. A. Khrapak, H. M. Thomas, and G. E. Morfill, Soft Matter **7**, 1287 (2011).

[26] V. A. Schweigert, I. V. Schweigert, A. Melzer, A. Homann, and A. Piel, Phys. Rev. E **54**, 4155 (1996).

[27] A. Melzer, A. Homann, and A. Piel, Phys. Rev. E **53**, 2757 (1996).

[28] R. Kompaneets, G. E. Morfill, and A. V. Ivlev, Phys. Rev. E **93**, 063201 (2016).

[29] O. S. Vaulina, I. I. Lisina, and E. A. Lisin, Europhys. Lett. **111**, 50003 (2015).

[30] J. Bartnick, A. Kaiser, H. Löwen, and A. V. Ivlev, J. Chem. Phys. **144**, 224901 (2016).

[31] G. E. Morfill and A. V. Ivlev, Rev. Mod. Phys. **81**, 1353 (2009).

[32] V. Nosenko, S. K. Zhdanov, A. V. Ivlev, C. A. Knapek, and G. E. Morfill, Phys. Rev. Lett. **103**, 015001 (2009).

[33] P. Hartmann, A. Douglass, J. C. Reyes, L. S. Matthews, T. W. Hyde, A. Kovács, and Z. Donkó, Phys. Rev. Lett. **105**, 115004 (2010).

[34] M. Rubin-Zuzic, G. E. Morfill, A. V. Ivlev, R. Pompl, B. A. Klumov, W. Bunk, H. M. Thomas, H. Rothermel, O. Havnes, and A. Fouquét, Nat. Phys. **2**, 181 (2006).

[35] S. A. Khrapak, G. E. Morfill, A. V. Ivlev, H. M. Thomas, D. A. Beysens, B. Zappoli, V. E. Fortov, A. M. Lipaev, and V. I. Molotkov, Phys. Rev. Lett. **96**, 015001 (2006).

[36] A. V. Ivlev, S. K. Zhdanov, H. M. Thomas, and G. E. Morfill, Europhys. Lett. **85**, 45001 (2009).

[37] C. Killer, T. Bockwoldt, S. Schütt, M. Himpel, A. Melzer, and A. Piel, Phys. Rev. Lett. **116**, 115002 (2016).

[38] P. Hartmann, M. C. Sándor, A. Kovács, and Z. Donkó, Phys. Rev. E **84**, 016404 (2011).

[39] Z. Haralson and J. Goree, Phys. Rev. Lett. **118**, 195001 (2017).

[40] V. Nosenko, A. V. Ivlev, and G. E. Morfill, Phys. Rev. Lett. **108**, 135005 (2012).

[41] V. E. Fortov, O. F. Petrov, O. S. Vaulina, and R. A. Timirkhanov, Phys. Rev. Lett. **109**, 055002 (2012).

[42] C. Yang, C.-W. Io, and Lin I., Phys. Rev. Lett. **109**, 225003 (2012).

[43] V. Nosenko, J. Goree, and A. Piel, Phys. Rev. Lett. **97**, 115001 (2006).

[44] S. Nunomura, S. Zhdanov, D. Samsonov, and G. Morfill, Phys. Rev. Lett. **94**, 045001 (2005).

[45] H.-W. Hu, W. Wang, and Lin I., Phys. Rev. Lett. **123**, 065002 (2019).

[46] E. V. Yakovlev, M. Chaudhuri, N. P. Kryuchkov, P. V. Ovcharov, A. V. Sapelkin, and S. O. Yurchenko, J. Chem. Phys. **151**, 114502 (2019).

[47] E. V. Yakovlev, N. P. Kryuchkov, P. V. Ovcharov, A. V. Sapelkin, V. V. Brazhkin, and S. O. Yurchenko, J. Phys. Chem. Lett. **11**, 1370 (2020).

[48] N. P. Kryuchkov, A. V. Ivlev, and S. O. Yurchenko, Soft Matter **14**, 9720 (2018).

[49] S. O. Yurchenko, E. V. Yakovlev, L. Couedel, N. P. Kryuchkov, A. M. Lipaev, V. N. Naumkin, A. Y. Kislov, P. V. Ovcharov, K. I. Zaytsev, E. V. Vorob'ev *et al.*, Phys. Rev. E **96**, 043201 (2017).

[50] E. V. Yakovlev, N. P. Kryuchkov, P. V. Ovcharov, K. Pitiot, A. V. Sapelkin, and S. O. Yurchenko, Phys. Rev. E **100**, 023203 (2019).

[51] L. Couedel, V. M. Nosenko, S. Zhdanov, A. V. Ivlev, I. Laut, E. V. Yakovlev, N. P. Kryuchkov, P. V. Ovcharov, A. M. Lipaev, and S. O. Yurchenko, Phys.-Usp. **62**, 1000 (2019).

[52] N. P. Kryuchkov, E. V. Yakovlev, E. A. Gorbunov, L. Couedel, A. M. Lipaev, and S. O. Yurchenko, Phys. Rev. Lett. **121**, 075003 (2018).

[53] G. Gogia and J. C. Burton, Phys. Rev. Lett. **119**, 178004 (2017).

[54] A. V. Ivlev and G. Morfill, Phys. Rev. E **63**, 016409 (2000).

[55] L. Couedel, V. Nosenko, A. V. Ivlev, S. K. Zhdanov, H. M. Thomas, and G. E. Morfill, Phys. Rev. Lett. **104**, 195001 (2010).

[56] A. V. Ivlev, S. K. Zhdanov, M. Lampe, and G. E. Morfill, Phys. Rev. Lett. **113**, 135002 (2014).

[57] J. A. Anderson, C. D. Lorenz, and A. Travesset, J. Comput. Phys. **227**, 5342 (2008).

[58] J. Glaser, T. D. Nguyen, J. A. Anderson, P. Lui, F. Spiga, J. A. Millan, D. C. Morse, and S. C. Glotzer, Comput. Phys. Commun. **192**, 97 (2015).

[59] P. Hartmann, G. J. Kalman, Z. Donkó, and K. Kutasi, Phys. Rev. E **72**, 026409 (2005).

[60] J.-P. Hansen and I. R. MacDonald, *Theory of Simple Liquids* (Academic Press, London, 2006).

[61] N. P. Kryuchkov, L. A. Mistryukova, V. V. Brazhkin, and S. O. Yurchenko, Sci. Rep. **9**, 10483 (2019).

[62] N. P. Kryuchkov, V. V. Brazhkin, and S. O. Yurchenko, J. Phys. Chem. Lett. **10**, 4470 (2019).

[63] S. O. Yurchenko, K. A. Komarov, N. P. Kryuchkov, K. I. Zaytsev, and V. V. Brazhkin, J. Chem. Phys. **148**, 134508 (2018).

[64] See Supplemental Material at http://link.aps.org/supplemental/10.1103/PhysRevE.101.063205 for supplemental movie illustrating strange attractors in the studied system.

[65] A. J. Lichtenberg and M. A. Lieberman, *Regular and Stochastic Motion* (Springer, New York, 1983).

[66] N. P. Kryuchkov, S. A. Khrapak, and S. O. Yurchenko, J. Chem. Phys. **146**, 134702 (2017).